2011

Measuring energy spectra of TeV gamma-ray emission from the Cygnus region of our galaxy with Milagro

Jessica G. Galbraith-Frew
Michigan Technological University

MEASURING ENERGY SPECTRA OF TEV GAMMA-RAY EMISSION FROM THE

CYGNUS REGION OF OUR GALAXY WITH MILAGRO

By

Jessica G. Galbraith-Frew

A THESIS

Submitted in partial fulfillment of the requirements for the degree of

MASTER OF SCIENCE

(Physics)

MICHIGAN TECHNOLOGICAL UNIVERSITY

2011

This thesis, "Measuring Energy Spectra of TeV Gamma-Ray Emission from the Cygnus Region of our Galaxy with Milagro," is hereby approved in partial fulfillment of the requirements for the degree of MASTER OF SCIENCE in Physics.

Department of Physics

Signatures:

Thesis Advisor _____

Dr. Petra Huentemeyer

Department Chair _____

Dr. Ravi Pandey

Date _____

Contents

List of Figures

List of Tables

Abstract

High energy gamma rays can provide fundamental clues to the origins of cosmic rays. In this thesis, TeV gamma-ray emission from the Cygnus region is studied. Previously the Milagro experiment detected five TeV gamma-ray sources in this region and a significant excess of TeV gamma rays whose origin is still unclear. To better understand the diffuse excess the separation of sources and diffuse emission is studied using the latest and most sensitive data set of the Milagro experiment. In addition, a newly developed technique is applied that allows the energy spectrum of the TeV gamma rays to be reconstructed using Milagro data. No conclusive statement can be made about the spectrum of the diffuse emission from the Cygnus region because of its low significance of 2.2 σ above the background in the studied data sample. The entire Cygnus region emission is best fit with a power law with a spectral index of α=2.40 (68% confidence interval: 1.35-2.92) and a exponential cutoff energy of 31.6 TeV (10.0-251.2 TeV). In the case of a simple power law assumption without a cutoff energy the best fit yields a spectral index of α=2.97 (68% confidence interval: 2.83-3.10). Neither of these best fits are in good agreement with the data. The best spectral fit to the TeV emission from MGRO J2019+37, the brightest source in the Cygnus region, yields a spectral index of α=2.30 (68% confidence interval: 1.40-2.70) with a cutoff energy of 50.1 TeV (68% confidence interval: 17.8-251.2 TeV) and a spectral index of α=2.75 (68% confidence interval: 2.65-2.85) when no exponential cutoff energy is assumed. According to the present analysis, MGRO J2019+37 contributes 25% to the differential flux from the entire Cygnus at 15 TeV.

Chapter 1

Introduction to High Energy Gamma-Ray Astrophysics in our Galaxy

1.1 TeV Gamma-Ray Astrophysics

1.1.1 Particles at the Highest Energies

Astrophysics is the study of the way objects outside our planet behave and interact. These objects range from large scale structures like super-massive blackholes to elementary particles. Physically traveling to sources and astrophysical objects outside our solar system is currently impossible, so to study those objects we study particles reaching Earth. One topic

of current interest in astrophysics is the study of nuclei, hadrons, and electrons at energies from 1 MeV to 100 EeV, known as cosmic rays. The sources of cosmic rays are difficult to study since cosmic rays are charged particles, and are deflected from their source by magnetic fields in our galaxy. One way to study cosmic rays, is to study particles they create in interactions while traveling from their source. Cosmic-rays can produce gamma rays at energies of over 1 GeV. Gamma rays are electromagnetic waves, or photons, at the highest energies of the electromagnetic spectrum. Because of their high energies they can only be created in the most extreme environments and interactions in the universe such as pulsars, supernovae, blackholes and very high energy cosmic-ray interactions. There are three main types of sources in observational gamma-ray astrophysics, point, extended, and diffuse. Gamma rays from point sources come from a particular object in the sky, such as a pulsar, and have an unresolved extension. Extended sources cover a small region of the sky, slightly larger than that of a point source. An example of a object that could appear as an extended source would be a supernova remnant. Diffuse emission comes from a large portion of the sky such as the galactic plane and its surroundings. There are a variety of processes that contribute significantly to the diffuse emission at GeV-TeV energies. First, gamma rays can be produced in a hadron-hadron interaction, where a hadronic cosmic ray hits another hadron, such as inside gas clouds or interstellar dust, between the source and the observer. This interaction creates secondary particles, among them there can be neutral pions which eventually decay into gamma rays. Second, gamma rays can be produced when a cosmic-ray electron scatters off a low energy photon, such as a photon from the

Cosmic Microwave Background (CMB) or Interstellar Radiation Fields (photons emitted by stars and other thermal processes). In this interaction, called Inverse Compton (IC) scattering, the photon carries away most of the energy and becomes a gamma ray. Third, Bremsstrahlung or braking radiation, is a process that is significant at GeV energies and drops off in the TeV energy range. In Bremsstrahlung, a gamma ray is produced by the acceleration and deflection of an electron in the electromagnetic field of another charged particle. These three processes contribute to the TeV diffuse emission in the galactic plane.

Gamma rays are not charged particles and therefore are not deflected by magnetic fields in the galaxy. Gamma rays point back to their source unlike cosmic rays. The study of gamma-ray emission can provide clues to cosmic-ray origins and better the understanding of cosmic-ray sources.

1.1.2 Cygnus Region

The Cygnus region is section of the night sky in the direction of the Cygnus constellation. Many of the objects seen in the Cygnus constellation are located in the Orion-Cygnus arm of our galaxy, which is the same arm that our solar system is located in. Figure 1.1 illustrates the arms of the Milky-Way.

The Cygnus region has been studied extensively because it contains many candidates for cosmic-ray and gamma-ray sources such as Wolf-Rayet stars, OB associations, pulsars,
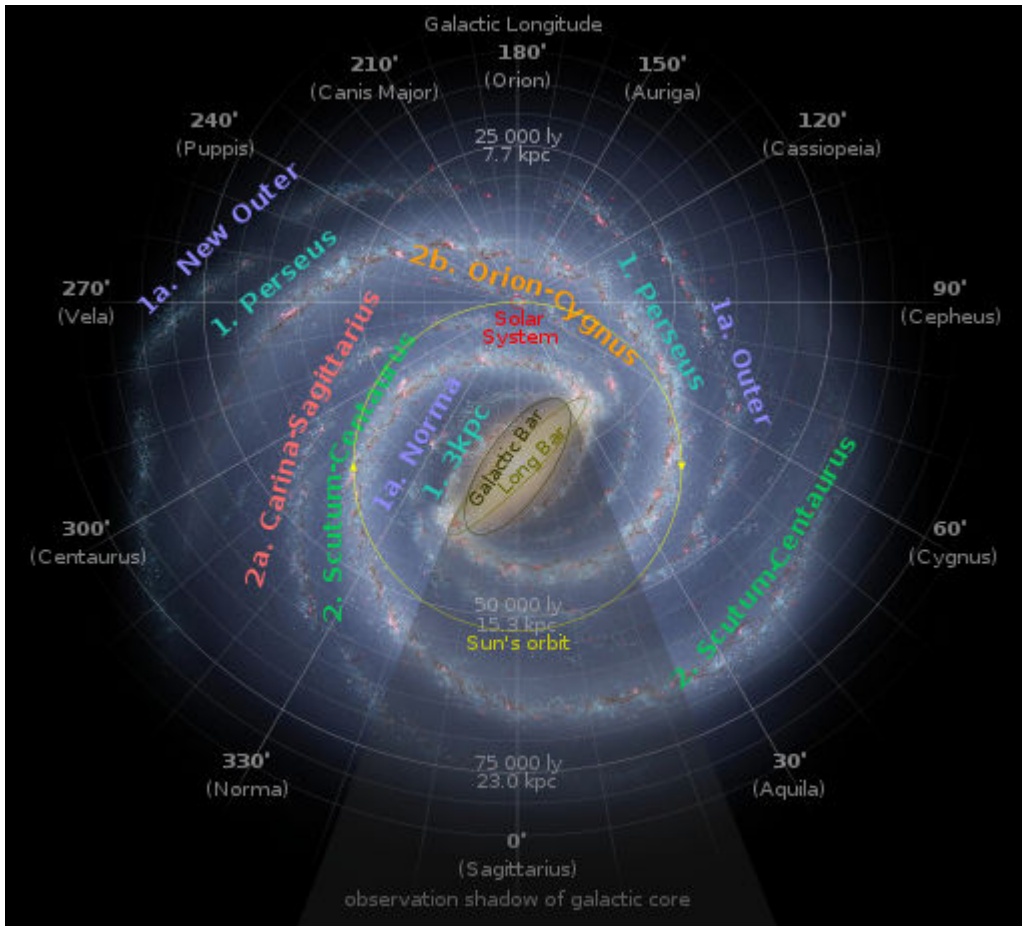
Figure 1.1: Diagram of the Milky-Way galactic arms illustrated from Earths perspective. Image taken from [1].

and supernova remnants. There is also a large amount of interstellar gas which is required for many of the interactions that produce gamma-rays [5]. The region has been studied in a wide range of wavelengths by different experiments including x-ray, infrared, and radio. Chandra, which studies the sky in the x-ray band, has surveyed the Cygnus region looking for lower energy counterparts to TeV sources and published a catalog of sources in the OB2 association which is one of the galaxies most massive star forming regions [6], [7]. In the radio range the Green Bank Telescope has studied the pulsar wind nebula

4

associated with TeV J2032+4130 [8]. There are numerous gamma-ray sources detected by experiments such as FERMI, EGRET, VERITAS, HESS, HEGRA, MAGIC, and Milagro. The first survey of Milagro detected two sources in the cygnus region MGRO J2019+37 and MGRO J2031+41 as well as a source candidate [9]. FERMI released a list of sources, two of which were associated with MGRO J2019+37 and MGRO J2031+41, as well as three unassociated sources in the Cygnus Region [10]. The Giant Metrewave Radio Telescope studied the region surrounding MGRO J2019+37 in radio frequency and infrared bands for sources. One source, PSR J2021+3651 has a wind nebula PWN G75.2+0.1 which could contribute to the flux of MGRO J2019+37 but it cannot explain the flux detected at TeV energies [11]. Recently VERITAS has performed an extensive study of the region, with 75 hours of exposure time. The data from that survey are still being analyzed but preliminary results indicate that the extension of MGRO J2019+37 is likely due to several unresolved sources in the region and may be associated with OB1 [9], [12]. The second source, MGRO J2031+41, has been detected by FERMI, MAGIC, and HEGRA.

There have been previous studies of the gamma-ray diffuse emission by various experiments throughout our sky. EGRET performed a extensive survey of the galaxy, and removed the known sources to study the diffuse emission [13]. HESS studied the diffuse emission from the galactic center ridge and found a spectra that was much harder than the local cosmic-ray spectra [14]. Extragalactic diffuse emission is often studied by telescopes because region can be selected with little contamination from other sources. FERMI studied the diffuse emission coming from a mid-latitude region of the sky and found that

the spectrum was 2.41±0.05, which is softer than the EGRET spectra of 2.13±0.03 [15], [16]. Studies of the emission along the galactic plane are made difficult by the presence of gamma-ray sources. Removing known sources can be difficult especially in regions like the Cygnus region which could contain several gamma-ray sources.

Estimating the diffuse emission reaching us from the various processes described above can be done with cosmic-ray propagation models. One such model, the galactic propagation (GALPROP) model is currently used because it predicts the gamma-ray emission for the entire galaxy. GALPROP is used to predict the gamma-ray emission in different areas of the sky by modeling the current understanding of the galactic magnetic fields, interstellar radiation fields, gas distributions, and the local cosmic-ray spectra. There are two versions of the GALPROP model which have been used by Milagro, the conventional model and the optimized model. The optimized GALPROP model was developed after EGRET measured the diffuse gamma ray flux, which showed an excess in TeV energies. The GALPROP model was optimized to better match EGRET by modifying the electron portion of the cosmic ray spectrum, making the IC component larger at higher energies [17], [18]. However, recent results published by the FERMI collaboration indicate the conventional model to be a better representation for diffuse emission [15], [19]. A previous study of the diffuse gamma-ray emission by Milagro showed two areas in the galactic plane which contain an excess of diffuse gamma-ray emission when compared to the optimized GALPROP model. In that study, the diffuse flux was obtained by removing the flux from the known sources in the region being studied leaving behind only diffuse emission [20], [9]. The diffuse flux

at 15 TeV was a factor of 2 times greater than the optimized GALPROP model and had a significance of 8.6 σ above the background [20]. Using the previous Milagro diffuse flux measurements and the conventional GALPROP model a new comparison was made. Figure 1.2 shows the flux profile plots. In the longitudinal profile, you can see that the measured flux exceeds that predicted by GALPROP in two regions, the Inner Galaxy ($35°<l<65°$) and the Cygnus Region ($65°<l<85°$). There are also two gaps in the diffuse flux, one from $29°$-$216°$, is outside the field of view of Milagro. The second gap from $111°$-$135°$ is not used because the analysis method was insensitive at those declinations. A second plot shown in Figure 1.2 is a latitudinal profile plot of the average flux from the Cygnus region going from ($-10°<b<10°$). Figure 1.3 shows the spectrum for each emission process predicted by GALPROP. The flux measured by Milagro is shown as a magenta point at 15 TeV, which was the median energy of the events used in the analysis. The flux of the previous Milagro diffuse excess is 7.5 times that of the conventional GALPROP model at 15 TeV. The red points are the diffuse flux measurements from EGRET. The diffuse event excess cannot be explained by the model alone, and indicates additional sources of gamma-rays, whether these are unresolved point or extended sources, contributions from cosmic-ray sources, or exotic dark matter processes [21], [22]. Measuring the energy spectrum of the emission can provide clues as to the source of the diffuse excess.
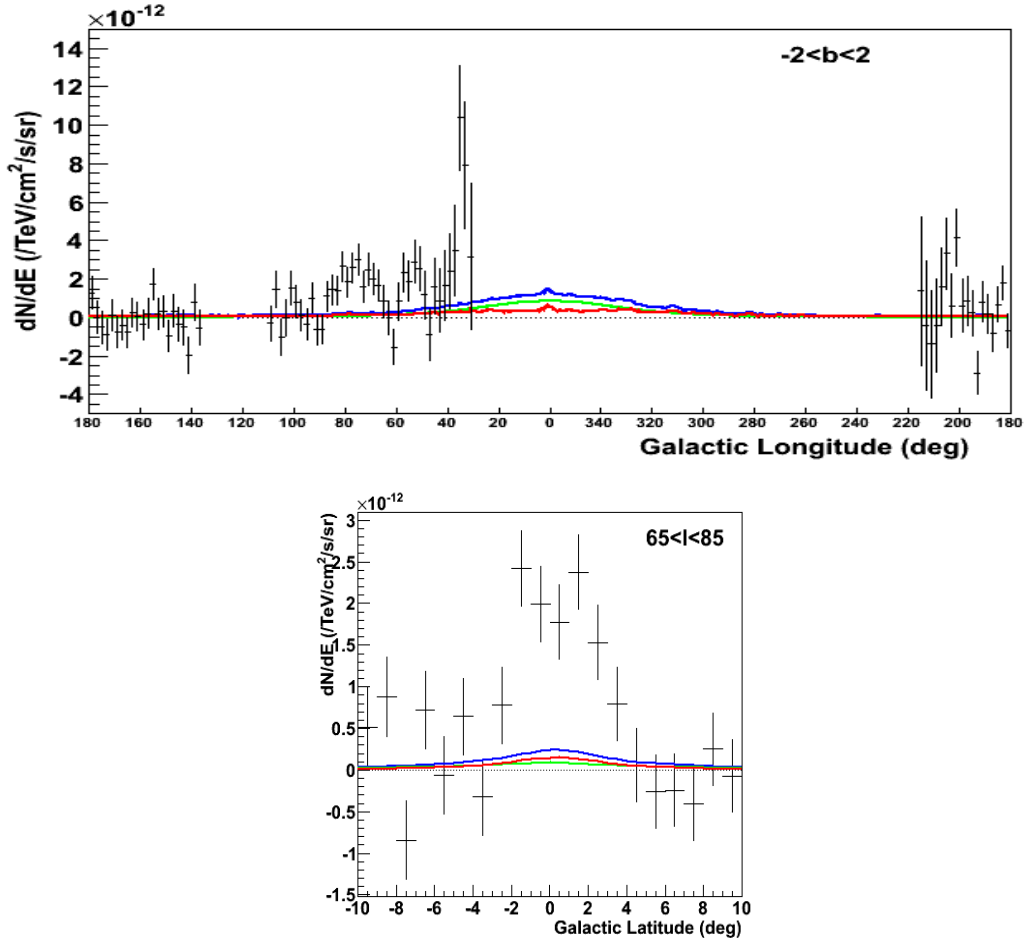
Figure 1.2: Diffuse flux profile plots comparing the average flux from Milagro with that predicted by the GALPROP contributions. Top: Profile of the diffuse flux within $\pm 2°$ of the galactic plane. Bottom: Latitude profile of the Cygnus region. The conventional GALPROP model predicted flux from different contributions are the colored lines. The red line is the flux from pion decay, the green line is the flux from the IC scattering, and the total from these two processes is the blue line. Not significant at these energies is bremsstrahlung.
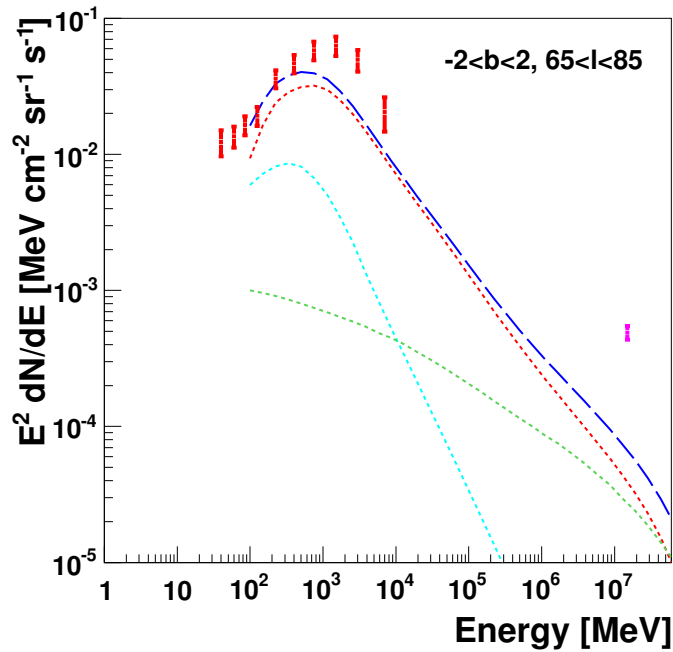
Figure 1.3: Energy spectrum of the diffuse gamma-ray emission from the Cygnus region. The red points are from EGRET, the magenta point is the flux measured by Milagro at 15 TeV. The conventional GALPROP predicted flux at different energies is shown for comparison as colored lines. The red line corresponds to the spectrum from pion decay, the green spectrum is from IC Scattering, the teal spectrum is from bremsstrahlung, and the combination is the dashed blue line.

1.2   Detection Techniques

There are two different types of gamma-ray detectors, space based experiments and ground based experiments. The main difference between these two methods comes from the fact that gamma rays cannot penetrate the Earth's atmosphere. Space based experiments detect the gamma rays before they interact with the atmosphere while ground based experiments detect the secondary particles created when gamma-rays enter the atmosphere.

9
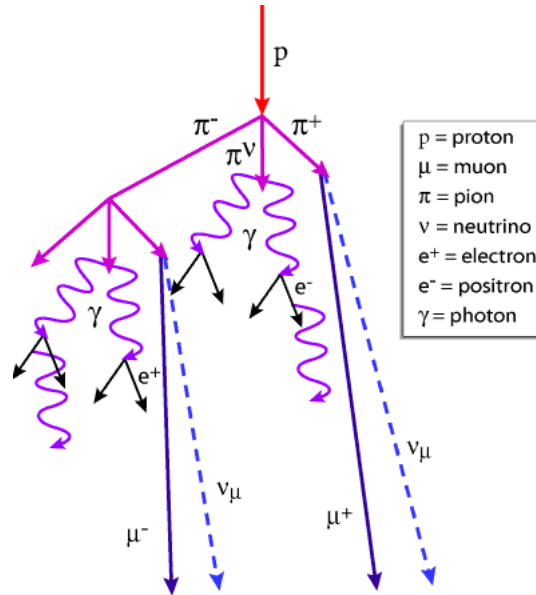
Figure 1.4: Diagram illustrating the processes that occur in a hadronic air shower. Neutral pions create smaller electromagnetic showers inside the hadronic air shower. Image taken from [2].

Spaced based experiments consist of detectors on satellite systems which are designed to convert the gamma-ray into an electron-positron pair. The path of the particles is tracked as they pass through the detector which is used to determine the direction of the gamma-ray. The detector includes a calorimeter which measures the energy of the particles. The final component of the detector is the anti-coincidence shield on the outside of the detector which is a scintillator that can distinguish between charged cosmic rays and gamma rays. Space based detectors have a smaller effective area but can view a wider range of the sky while in orbit.

Once a gamma-ray enters the atmosphere, it will interact with the particles in the atmosphere and create a shower of secondary particles, called an extensive air shower (EAS).

There are two main types of particle interactions that take place in an EAS, and can be seen in Figure 1.4; electromagnetic interactions and hadronic interactions. There are two main electromagnetic interactions that take place during the shower. A photon can undergo pair production if it has enough energy and create an electron-positron pair. Additional photons are then produced via bremsstrahlung, as the high energy charged particles like electrons pass by another charged particle. An EAS created by a hadron involves both hadronic interaction and electromagnetic interactions. In a hadronic interaction mesons are produced. Charged pions create their own smaller showers which contain muons and neutrinos. Neutral pions decay into gamma rays and create an electromagnetic shower. By the time an EAS reaches the ground level it mainly consists of positrons, electrons and photons.

There are two forms of surface gamma-ray detectors which detect secondary particles from EAS. Imaging Air Cherenkov Telescopes (IACT) are designed to detect Cherenkov light produced by the charged particles in the EAS. Cherenkov radiation is produced when a charged particle travels through a medium at a speed greater than the speed of light in that medium. IACTs use mirrors to focus the Cherenkov photons from EAS onto an array of PMTs. These telescopes are limited in operation time due to the large amount of background light created by the moon, stars, and sun. They also only view a small portion of the sky at a time. The second ground detector is called an EAS Array which detect the secondary particles when they hit the ground. This can be done in two ways. The first method developed to detect the particles involves an array of scintillator detectors. These devices absorb the incoming particles and reemit the energy as a photon. Another ground based

detection method was used in the Milagro experiment. Milagro was the first experiment that successfully used an array of water Cherenkov counters to detect gamma rays. Water Cherenkov detectors are designed to detect Cherenkov photons emitted by secondary EAS particles in the water. Details of the Milagro detector are described in the next chapter.

Chapter 2

The Milagro Observatory

The Milagro Observatory was a ground based water Cherenkov detector located near Los Alamos, New Mexico, at an altitude of 2630 m and coordinates of 35° 52' 45"N latitude and 106° 40' 37"W longitude. The observatory was operational from July 2000 - January 2008 during which time it continuously monitored a large portion of the Northern Hemisphere's TeV gamma-ray sky [23]. While it was in operation, the observatory detected particles generated by cosmic-ray and gamma-ray air showers with energies between 0.1-100 TeV[23].

The detector originally consisted of a pond that measured 80 m x 60 m x 8 m, and contained a total of 723, 20-cm diameter Hamamatsu (#R5912SEL) photomultiplier tubes (PMT). These PMTs were arranged in two layers. The upper layer which is referred to as the air

Figure 2.1: Overhead view of the Milagro pond. Image taken from [2].

shower layer had 450 PMTs and was primarily used to reconstruct the air showers. The PMTs of this layer were located 1.5 m below the waters surface. The lower layer, with the PMTs at a depth of 6 m, is referred to as the muon layer and contained the remaining 273 PMTs [23], [3]. High energy electrons and positrons from the EAS will emit Cherenkov light inside the water tanks. These photons are collected by the PMTs in the air shower layer. By the time the shower reaches the muon layer at the greater depth, most of the electrons and positrons have been absorbed leaving behind heavier particles such as muons. The muon layer was used primarily to distinguish between gamma-ray and hadronic cosmic-ray air showers, because hadronic air showers create significantly more muons than gamma-ray air showers [24]. The muons will produce Cherenkov light signals in the muon layer PMT.

14
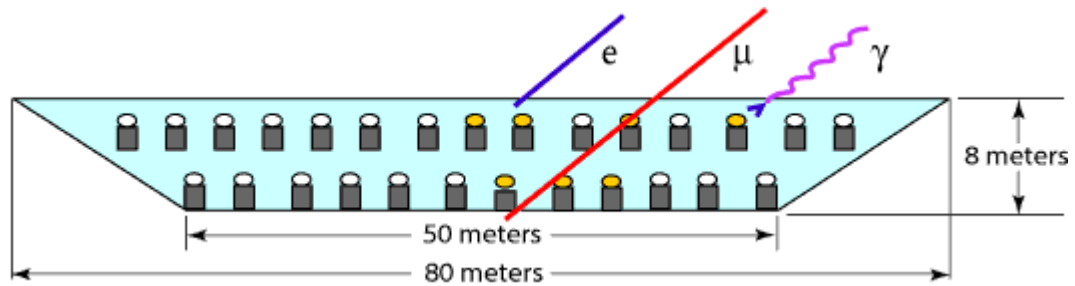
Figure 2.2: Schematic of the interior of the Milagro pond demonstrating the interactions that occur inside the detector. Incoming electrons and positrons will emit Cherenkov light and be absorbed before reaching the muon layer. Incoming muons will create Cherenkov light through the entire detector. Incoming gamma rays will pair produce and create an electron-positron pair. Image taken from [2].

Figure 2.2 illustrates the roles of the two layers. Each PMT had a upward pointing cone, or baffle on it to collect more photons, and to keep down contamination from photons being reflected off of other surfaces, and from Cherenkov photons produced by muons from showers traveling near horizontal angles.

In 2004 the detector was expanded to an area of 40000 m^2 by adding an array of 175 outrigger water tanks with a height of 1 m and a diameter of 2.4 m, each containing a downward facing PMT located at the top of the tank [3]. Figure 2.3 shows the locations of the outrigger tanks surrounding the central pond. The larger detector area increased the sensitivity of the observatory.

Figure 2.3: Overhead view of pond with red markers where tanks were placed in 2004. Image taken from [3].

2.1 Event Triggering

Signals from PMTs were analyzed by a data acquisition system (DAQ) to determine whether or not they were true air shower events. If the signal passes the trigger conditions it is considered an event. During the course of the lifetime of the observatory there were two different trigger conditions for signals. The first method used from the beginning of the experiment to March 2002, was the multiplicity trigger, which is a measure of the number of PMTs hit in the air shower layer over a certain period of time (200 ns) [3]. If the number of PMTs hit is above a certain threshold (usually 50-70 PMTs), then the PMT signals are considered an air shower event. In 2002, the triggering was improved by adding a programmable Versa Module Europa (VME) trigger card to the DAQ. The VME allowed the risetime of the signals to be calculated and was used in determining whether or not the

signals corresponded to an event. Risetime is a measure of how fast signals come in, and is the amount of time it takes for 10%-90% of the events signals to arrive. Particle shower events will produce signals arriving at the same time, while noise will be random hits. The risetime trigger gives the advantage of being able to lower the detector threshold while still being able to distinguish muon events traveling horizontally from other events. Signals from PMTs were then used to reconstruct where the air shower came from in the sky. The VME card was used until it failed in April 2006 and the triggering system went back to a multiplicity trigger. These events are then weighted and placed into final skymaps which are described in the next section.

2.2   SkyMaps

Skymaps are the final form of the Milagro data. They consist of data binned by an energy parameter and location of the event in celestial coordinates. The skymaps are binned in 0.1x0.1 deg bins and cover the entire visible range of the detector in right ascension and declination.

2.2.1 Reconstruction of Events

On a daily basis Milagro collected ~250GB of raw data, which if it was all reconstructed and stored would reach over 82TB of disk space a year [23]. Because storing such a large amount of data was not feasible at the time, only reconstructed parameters were stored for each event with a few exceptions. Raw data from certain areas like the Crab Nebula, the Sun, and the Moon location were stored. Raw data was also saved when Milagro received notification from other experiments that events like GRBs or AGN flares were happening [3]. The rest of the raw data was reconstructed and only the reconstructed parameters were saved. There were two main steps in the online reconstruction of the events, which was done in real time.

The first step in the reconstruction of events is the core reconstruction. The core position is the place where the primary particle would have landed had it not interacted in the atmosphere. The PMTs near the core position will measure the highest concentration of particles and have the most photoelectrons (PEs). If the core lands on the pond, then the core position is just the weighted center of mass, where the position is weighted by the square-root of number of PEs detected. If the core lands off the pond, the position is harder to calculate. In that case it was assumed that the core position was 50 m from the center of the pond. When the outrigger tanks were added to the pond, they were used in addition to the air shower PMTs to reconstruct the core position.

The next stage in the reconstruction process is to determine the direction that the particle originated from in the sky. This is done by using the relative arrival times of the PMT signals to reconstruct the shower front. The orientation of the shower front gives an angle, which corresponds to a position in the sky. To accurately determine the direction of the air shower the time response of the PMT must be calibrated because the angular reconstruction requires correct timing for the PMT hits. The calibration system used a laser to send light into the water to test the timing of each PMT. This allows for the measuring of how long it takes the light to reach the PMTs and the response time for the electronics. Another correction must be performed on the shower front due to the curvature of the air shower front. The PMT arrival times are adjusted based on the curvature of the front and the correction depends on the distance of the PMT from the core position. A fit is done to the shower plane after correcting for the curvature of the shower front which gives the shower direction. Using the best fit, a predicted arrival time is calculated for each PMT. PMTs that are not calibrated correctly will have arrival times that are not the same as the predicted arrival times. The difference between the prediction and the arrival times can be used to calibrate the PMT if they are consistently off. The angular reconstruction is preformed again after removing the PMTs not properly timed until the fit does not improve.

2.2.2 Background

Milagro receives signals produced by cosmic-ray and gamma-ray air showers. Cosmic-ray showers are similar to gamma-ray showers and create background events that need to be separated from gamma-ray events. In order to enhance the gamma-ray to cosmic-ray event ratio a weight is applied based on the probability that an air shower was produced by a gamma ray. The weight applied is based on the A5 parameter, which had been derived previously in Monte Carlo studies [3]:

$$A_5 = \frac{f * F_{fit}^{cor}}{MaxPE_{MU}}$$

Here f is the energy parameter (described below in section 2.2.3) which tends to increase with energy, F_{fit}^{cor} is the fraction of PMTs used in the reconstruction fits and the $MaxPE_{MU}$ is the maximum number of PEs collected by a PMT in the muon layer for an event. Cosmic-ray events have a higher number of PEs in the muon layer due to the fact that they contain many more muons than gamma-ray air showers. Each event is weighted based on its A5 value and placed into skymaps. Applying a weight instead of a cut on A5 increases the sensitivity of Milagro by using all the events collected.

After the events have been weighted to enhance the gamma-ray signal, the gamma-ray source ("on") and background ("off") are determined. Traditionally the background is estimated by examining the event rate in the sky around a source candidate and subtracting

20

this rate from the source area rate [25]. Creating a background skymap for Milagro requires changes to the method as Milagro views the entire sky at the same time. The method is called direct integration and allows for the estimation of the gamma-ray background. In this process it is assumed that for a 2 hour interval the background trigger rate is the same at every location, and that the only thing that changes with coordinates is the efficiency of the detector. Using this an efficiency map is calculated, which is the probability an event came from a certain position. The details of the integration of the efficiency map are given in Atkins,R. 2003 [26]. The final skymap file contains a signal map, a background map, and a significance map calculated according to the method of Li & Ma [25].

2.2.3   Energy Reconstruction

Gamma-rays interact when they hit particles in the atmosphere, so directly measuring the primary gamma-ray's energy is not possible. Using Monte Carlo simulations however, the energy of the primary gamma-ray can be estimated. Gamma rays were simulated for energies from 5 GeV-2000 TeV to get a relation between energy and the detector response [4]. The program CORSIKA simulates the air shower created by the primary particle to the altitude of the detector at 2630 m [27]. The output from the CORSIKA simulation is read into Geant4 which simulates response of the Milagro detector to the secondary particles created in the air shower [28]. The simulated events are then weighted to correct for simulation biases. The weights correct for the throw radius bias, the primary species

bias, and the assumed spectrum. The simulated events have a known energy and a simulated detector response. This gives a relationship between the number of PMTs hit to the energy of the gamma-ray. Air showers with more energy are expected be larger than low energy air showers and therefore the number of PMTs hit is related to the showers energy. The Milagro energy parameter is:

$$f = \frac{N_{AS}}{N_{AS}^{live}} + \frac{N_{OR}}{N_{OR}^{live}}$$

where N_{AS} is the number of air shower PMTs hit, N_{AS}^{live} is the number of operational PMTs in the air shower layer, N_{OR} is the number of outrigger PMTs hit, and N_{OR}^{live} is the number of operational PMTs in the outrigger tanks. The first term is the fraction of air shower layer PMTs hit and the second term is the fraction of outrigger tank PMTs hit. f is a sum of two fractions with values between 0.0 and 2.0. Showers that have low energy have a small f value while showers with high energy have a larger f value.

MILAGRO skymaps are binned based on the f value of the event. There are 10 f bins, but the lowest f bin is not used so that the analysis is insensitive to small changes in the triggering threshold. Figure 2.4 shows the distribution of energies for each f bin from simulated gamma ray showers.

There is large overlap between the f bins which comes from the fact that there are other factors that are not taken into account, such as the height at which the primary interacts with the atmosphere or its zenith angle with respect to the detector plane. The mean energy for each f bin is given in Table 2.1.
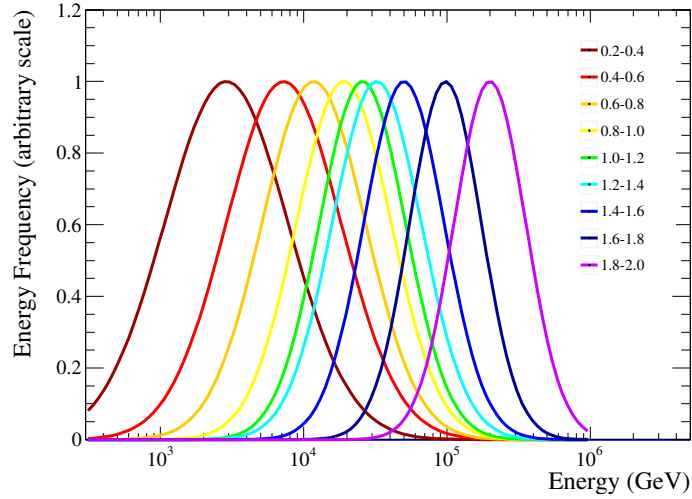
Figure 2.4: *f* energy distributions based on simulated showers. Image taken from [4].

Table 2.1

Mean energy of each *f* bin from MC simulation assuming a spectrum with a photon index of -2.60 without a cutoff energy at a certain energy.

Mean Energy (TeV)								
0.2-0.4	0.4-0.6	0.6-0.8	0.8-1.0	1.0-1.2	1.2-1.4	1.4-1.6	1.6-1.8	1.8-2.0
3.02	6.03	10.47	15.14	22.39	35.48	52.48	89.13	229.09

2.2.4 Angular Resolution

The angular resolution of the detector is determined by performing a 2 dimensional Gaussian fit to the location of the crab nebula which is seen as a point source in the Milagro event excess maps. The crab nebula is the result of a supernova explosion that left behind a pulsar. The position is well known due to intense study by many observatories and is often used for calibration. Table 2.2 gives the angular resolution of each *f* bin for the data being

Table 2.2

Angular resolution of each f bin

Angular Resolution of Detector (σ)									
0.0-0.2	0.2-0.4	0.4-0.6	0.6-0.8	0.8-1.0	1.0-1.2	1.2-1.4	1.4-1.6	1.6-1.8	1.8-2.0
2.00	0.74	0.60	0.51	0.44	0.40	0.37	0.37	0.31	0.37

used in the analysis.

The angular resolution of the detector improves with f bin. Higher energy events hit more PMTs which allows for a better reconstruction of the direction. The angular resolution is important in being able to separate sources from diffuse emission.

Chapter 3

Analysis Technique

For this analysis the most recent Milagro data was used from the last 2.5 years of operation. The Cygnus region of the galactic plane is for this analysis considered to extend from $65°$ to $85°$ galactic longitude, and $-2°$ to $+2°$ galactic latitude.

In order to find the energy spectrum of measured gamma rays a fitting technique described in this chapter is used. Two commonly assumed functions to describe TeV gamma-ray spectra are a simple power law or a power law with an exponential cutoff energy:

$$\frac{dN}{dE} = I_o \left(\frac{E}{E_o} \right)^{-\alpha} \qquad or \qquad \frac{dN}{dE} = I_o \left(\frac{E}{E_o} \right)^{-\alpha} e^{\frac{-E}{E_c}}$$

where α is the spectral index which describes the slope of the curve, I_o is the flux normalization parameter, and E_c is the cutoff energy. These three values are the parameters found

in the fitting procedure.

In order to derive the spectral parameters for a source a chi-squared (χ^2) fit is performed. χ^2 is calculated as follows:

$$\chi^2(I_o, \alpha, E_c) = \sum_{i=f} \frac{(P_i(I_o, \alpha, E_c, Declination) - M_i)^2}{\delta P_i^2 + \delta M_i^2} = \sum_{i=f} \chi_i^2$$

Here M_i is the measured number of weighted events per day and P_i is the number of weighted events per day predicted by Monte Carlo simulations in each f bin i. δM_i and δP_i are the uncertainties in each rate for a particular spectrum. χ^2 values for a variety of spectra are calculated and the parameter value set that yields the minimum χ^2 value represents the spectral assumption that best fits the data.

M_i is calculated from the Milagro skymaps where the measured events are weighted based on the A5 parameter and binned according to their f value. For this analysis two different types of skymaps were used. Unsmoothed skymaps contain the A5 weighted number of events in 0.1 x 0.1 deg bins in celestial coordinates while smoothed skymaps contain A5 weighted events that have been spread out according to the Milagro point-spread function. P_i is calculated for a range of values of the spectral parameters α, E_c and I_o thus weighting simulated events representing a new spectral assumption every time.

The spectral parameters form a 2 dimensional space in case of the simple power law assumption and a 3 dimensional space in case of the spectral assumption including an expo-

Table 3.1

Range of parameter values for spectral assumptions and step sizes of the parameter space scan.

Parameter Ranges		
Parameter	Range	Step Size
α	0.50-4.50	0.025
P_o	0.00-10.00	0.040
Log(E_c)	3.00-6.00	0.050

nential cut-off. The range of parameter values and the step size of the scan is given in Table 3.1

The spectral index range was chosen based on commonly measured sources spectra. The cutoff energy range goes from 1 TeV to 1000 TeV which extends beyond the sensitivity range of Milagro at 100 TeV [23]. The parameter P_o is the fraction of the flux normalization of the crab nebula at 10 TeV as measured by HESS assuming no cutoff energy [29].

The declination dependence of P_i comes from the fact that the exposure time of sources at different declinations is different, as well as changes in the effective area of the detector. The sensitivity of Milagro changes with declination. Figure 3.1 shows the variation in P_i at different declinations of the region. The value of P_i varies between +5% and -15% of the value of P_i at 36 deg across the Cygnus region.
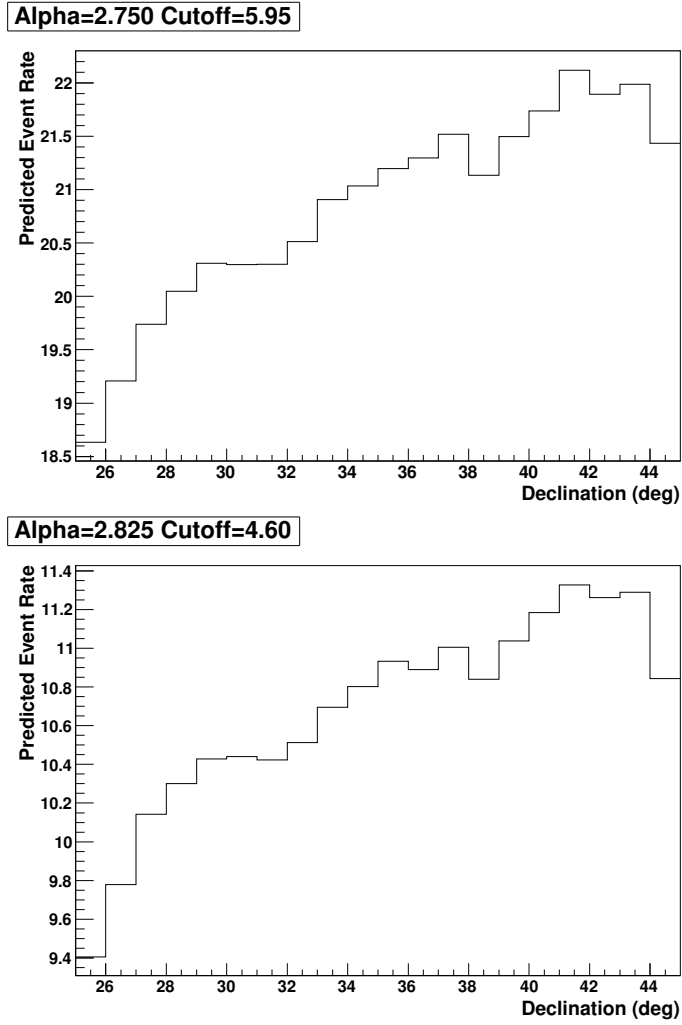
Figure 3.1: Plot of variation of P_i at different declinations across the cygnus region assuming a certain spectrum

Chapter 4

Results

There are four sources and one on the boundary of the region that were detected by Milagro with a pretrial significance of $> 4 \, \sigma$ above the background. They are listed in Table 4.1. Two of the sources were found in the earlier Milagro sky surveys and were taken into account in the first Milagro diffuse analysis [20]. Using the Fermi catalog a new survey was done looking for excesses at the location of the Fermi sources. Three more sources were found during this survey and are listed in Table 4.1 [10].

A smoothed map of the significance of the region is shown in Figure 4.1 with the four sources in the region marked. The spectral fitting procedure was applied to the entire region combining diffuse emission with point and extended sources, and the brightest source, MGRO J2019+37. Spectral fits to the diffuse excess from the Cygnus direction are also

Table 4.1
Sources in the Cygnus region from previous Milagro searches.
Counterparts listed are the other possible names for the source. *Source is
on edge of region.

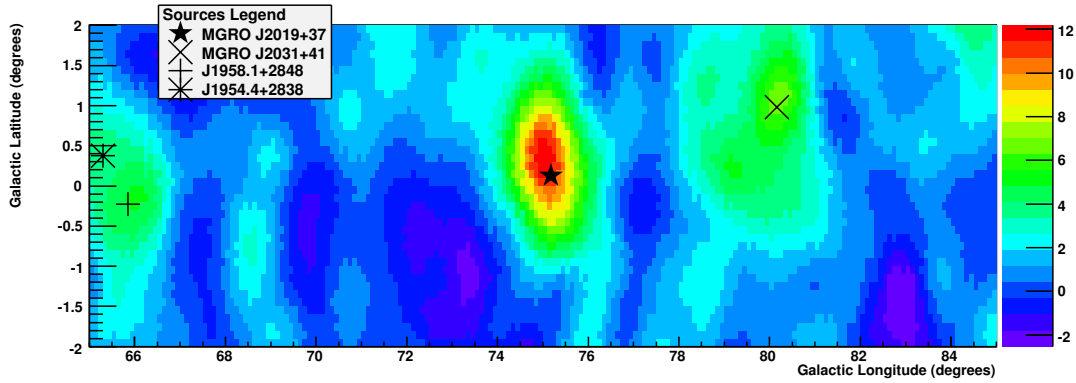| Sources in Cygnus Region					
Name	l (deg)	b (deg)	Flux (x10^{-17} TeV^{-1} s^{-1} cm^{-2})	Significance	Counterparts
J1954.4+2838	65.30	0.38	37.1 ± 8.6	4.3	-
J1958.1+2848	65.85	-0.23	34.7 ± 8.6	4.0	-
MGRO J2019+37	75.18	0.13	108.3 ± 8.7	12.4	J2020.8+3649
MGRO J2031+41	80.16	0.98	63.3 ± 8.3	7.6	TEV 2032+41, J2032.2+4122
J2021.5+4026*	78.23	2.07	35.8 ± 8.5	4.2	-

Figure 4.1: Significance Map of the entire Cygnus Region, with sources
from Table 4.1 marked

attempted but not successful because the significance of the diffuse emission excess is not

sufficient. Studies aimed at an efficient and clean separation between diffuse and source

emission in the Cygnus region will be presented nonetheless.

Table 4.2

Fit results for the average emission from the Cygnus region

Fit Parameters for Entire Region						
Fit	α	I_o (x10^{-10} TeV^{-1} s^{-1} m^{-2})	E_c (TeV)	χ^2	DOF	Probability
W/ Cutoff	2.40 (1.35-2.92)	28.95 (15.69-80.71)	31.62 (10.00-251.18)	11.99	6	6.2%
W/O Cutoff	2.97 (2.83-3.10)	15.04 (12.45-17.95)	-	17.03	7	1.7%

4.1 The Cygnus Region Spectrum

Using an unsmoothed skymap M_i was calculated by summing the number of weighted events in each bin of the sky over the entire range and dividing by the duration of the data taking period corresponding to the final and most sensitive 906 days of Milagro data. In the simulation a declination of $36°$, which corresponds to the center of the region, was used. The significance of the region in this data including localized sources is 7.6 σ above the background. Table 4.2 shows the best fit parameters for the fit with both a cutoff energy and no cutoff energy.

Figure 4.2 shows the projections of the χ^2 histogram for each parameter. The figures show 1-5 σ contours surrounding the minimum χ^2 value. The error ranges for each parameter come from the maximum and minimum parameter values for the 1 σ contours.

Figure 4.3 shows the f distributions for both fits, the data distribution in blue and the Monte Carlo simulation corresponding to the best fit parameters in yellow. The Cygnus region contains a number of different sources that contribute to the emission spectrum of the entire region. This variation in the spectrum across the region contributes to the
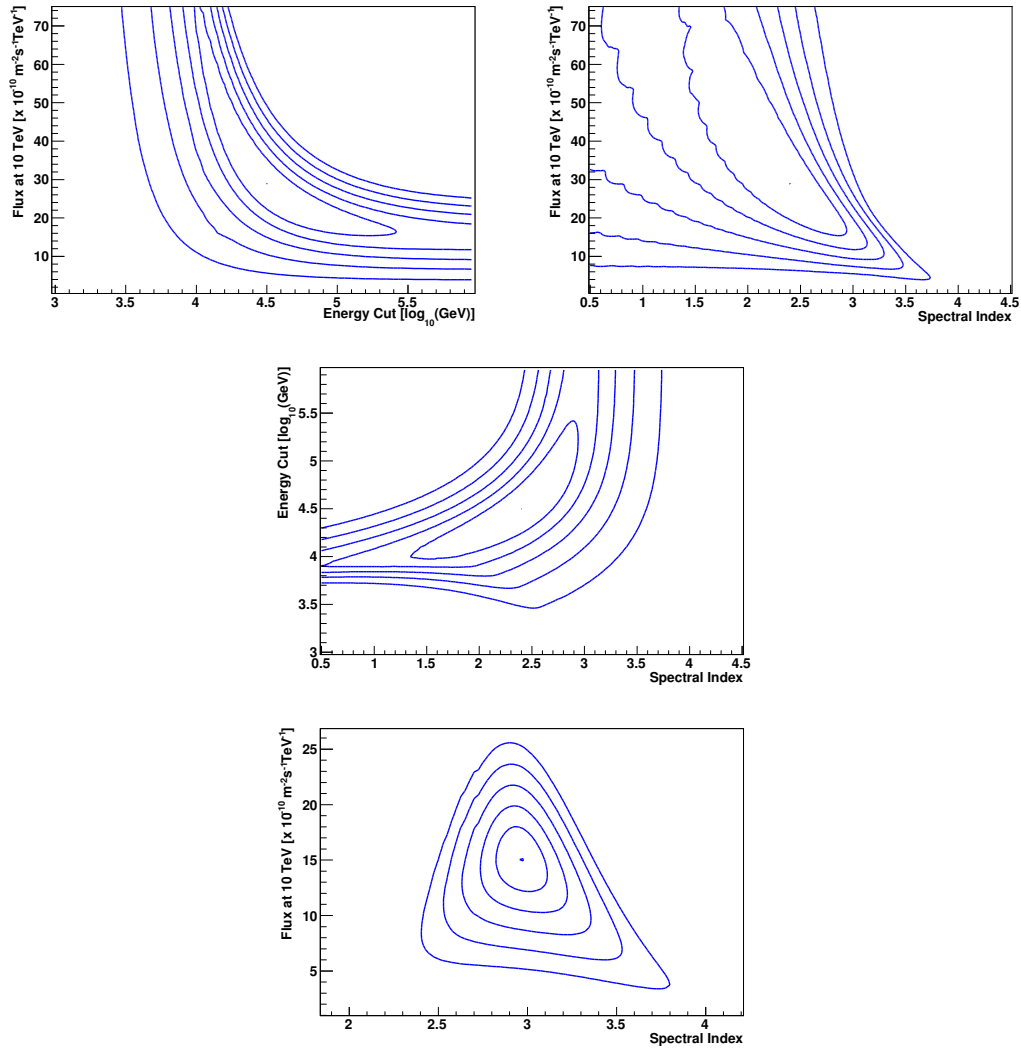
Figure 4.2: Projections of the 3 dimensional χ^2 space for the entire Cygnus Region. Top/Middle: Projections for each parameter assuming a cutoff energy. Contours show the change of χ^2. Bottom: Projection assuming no cutoff energy.

uncertainty of the fit because different sources have different emission spectra.

The spectrum of the region for the best fit in both cases is shown in Figure 4.4 along with the 1 and 2σ error bands and the previous Milagro diffuse measurement at 15 TeV. The
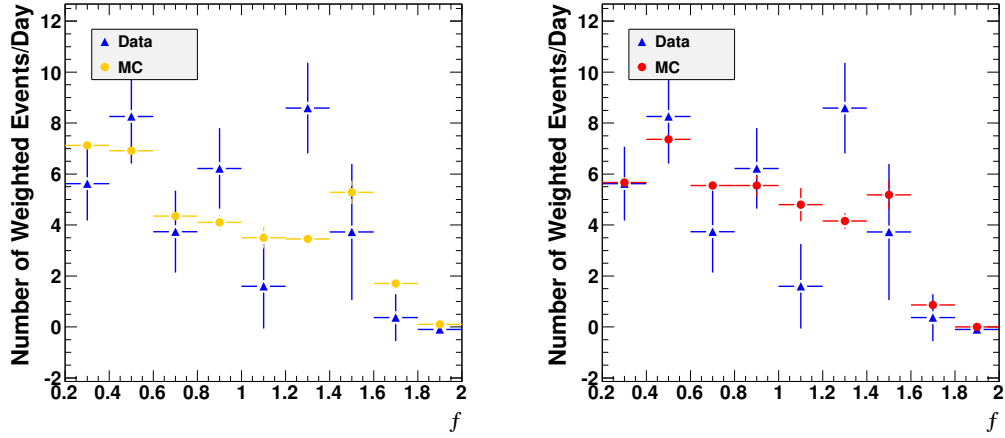
Figure 4.3: f distribution for entire Cygnus region. Left: Data event rates and Monte Carlo event rates for the best fit without a cutoff. Right: Data event rates and Monte Carlo event rates for the best fit with a cutoff.

average diffuse flux measurement has both the statistical uncertainty as a black error bar and the red error bar is the combined statistical and systematic uncertainties.

The flux of the Cygnus region and the flux of the previous diffuse emission is nearly equivalent at 15 TeV. This is unexpected because the diffuse measurement does not include the two largest sources from the region. There are several differences between the analysis which could contribute to this discrepancy. First of all the data used by the two values differs. The diffuse analysis used an earlier Milagro data set which contained data from before the addition of the outrigger tanks and was of longer duration. Second, the previous diffuse emission analysis assumed a spectrum of $E^{-2.75}$ to calculate the differential flux at 15 TeV while the goal of the present analysis is to derive the best spectral fit to the entire region (that also contains a variety of sources contributing to the spectrum) [20]. The re-
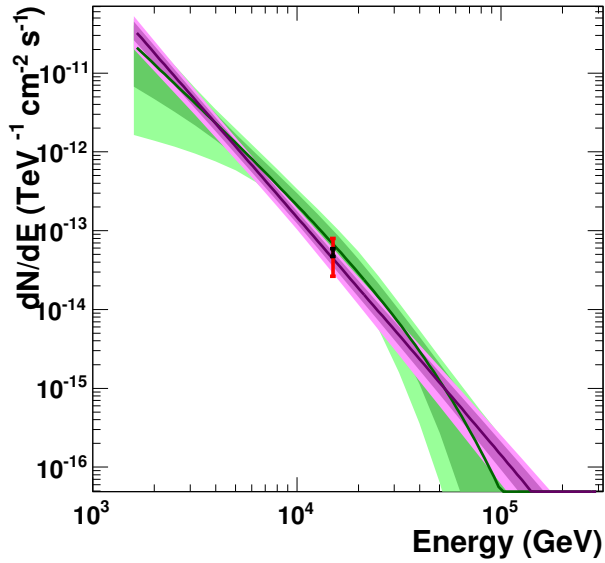
Figure 4.4: Spectrum of the entire Cygnus Region with 1 and 2 σ error bands around best fit. Purple: Fit without cutoff energy. Green: Fit with cutoff energy. The black point is the Milagro diffuse measurement with error bars for statistical uncertainty (black) and the combined statistical and systematic uncertainties (red).

sulting indices from the best fit without a cutoff or with a cutoff are 2.97 and 2.40. Third, the previous diffuse analysis took into account the changing sensitivity of the Milagro detector with declination, which has not yet been done for the present analysis of the entire region. Here a single declination of 36 deg was assumed for the whole region spanning 20 deg between 25 and 45 deg.

To investigate this further, systematic studies were performed by varying the declination used in the Monte Carlo simulations. The results of the fits for declinations 25 deg and 45 deg are given in Table 4.3.

Table 4.3

Results of the declination study preformed on the Cygnus region

Fit	α	I_o (x10^{-10} TeV^{-1} s^{-1} m^{-2})	E_c (TeV)	χ^2	DOF	Probability
Declination-45°						
W/ Cutoff	2.38 (1.40-2.92)	28.95 (15.69-78.45)	31.62 (10.00-251.18)	11.19	6	8.2%
W/O Cutoff	2.97 (2.85-3.10)	15.37 (12.45-17.95)	-	16.33	7	2.2%
Declination-25°						
W/ Cutoff	2.48 (1.35-2.92)	32.51 (19.25-80.71)	35.48 (11.22-199.53)	9.81	6	13.2%
W/O Cutoff	3.00 (2.88-3.13)	17.95 (14.72-21.19)	-	15.35	7	3.2%

The variation of the parameters at the declinations farthest from the center of the region are still within the errors of the original parameters. The overall flux of the fits at 15 TeV slightly higher for a declination of 25 degrees, but the overall difference is small between the fits. The probabilities of the Cygnus region fits show that the region cannot be fit by a single power law spectrum.

4.2 Diffuse Emission

In order to study the diffuse emission the known sources must be separated from the diffuse emission. A region around each of the sources listed in Table 4.1 was cut out of the skymap. These regions excluded from the measured number of events are referred to as exclusion regions. A variety of studies were done by varying the exclusion region around each of the sources in order to effectively separate the diffuse emission from the sources. Figure 4.5 shows the smoothed skymaps where each map is calculated based on the events in one f bin.
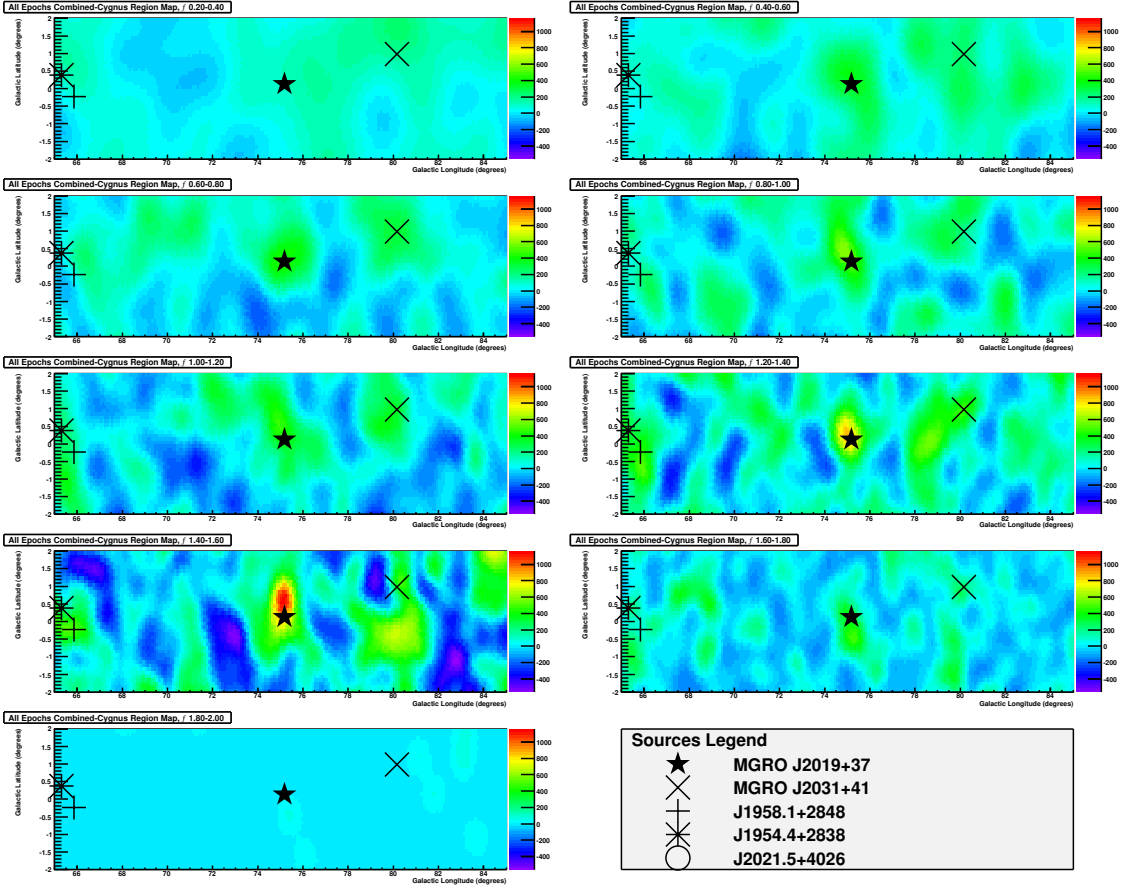
Figure 4.5: Smoothed maps of the entire Cygnus region, each plot representing one f bin.

The first study that was done, was assuming a fixed size for the exclusion region. A binsize of $3°$x$3°$ around the point sources was chosen based on the angular resolution of the detector. A fixed exclusion region of $\pm1.5^o$ was used to cut out point source gamma-rays, and is shown in Figure 4.6 The remaining events were considered to be from diffuse emission. The significance of the remaining excess was calculated to be 2.0 σ above the background, which is not significant enough for a spectral analysis. This indicated that too much diffuse emission was excluded.
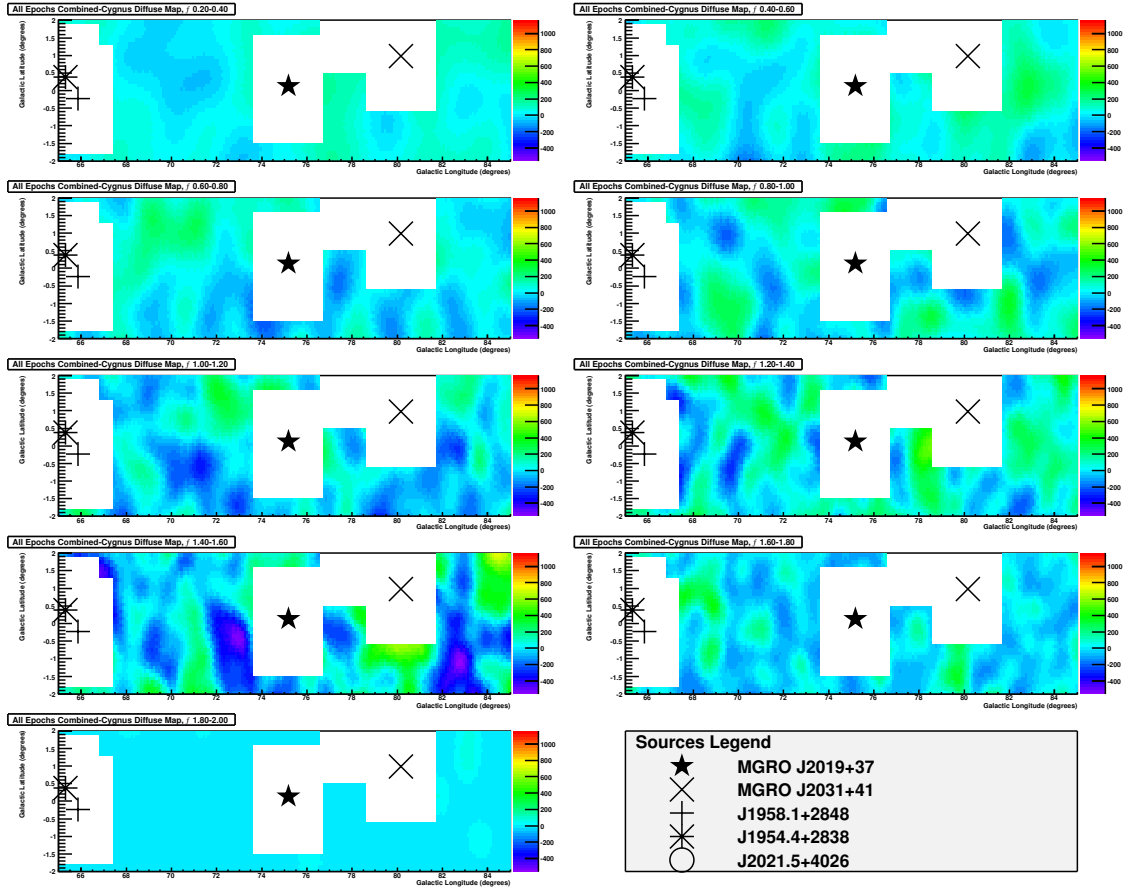
Figure 4.6: Smoothed map of the enter Cygnus region binned by f with fixed exclusion regions

To improve the separation between sources the fact that the angular resolution of the detector improves with increasing energy (see Table 2.2) was used to calculate the size of the exclusion region. At lower energies (f values) the resolution of the detector is worst so the exclusion region will be larger while at higher energies the angular resolution is better so a smaller exclusion region can be used. The optimal exclusion region size is calculated by computing the significance above background for a point source at different distances from the source location. The maximum significance of the signal over background occurs

Figure 4.7: Smoothed map of the entire Cygnus region for the nine f that were used in the analysis. The source exclusion region sizes become smaller for higher f bins reflecting the better detector resolution at higher energies.

at $d=2.8 \times \sigma$ deg, where d is side of a square exclusion region and σ is the resolution. With increasing f bins the size of the exclusion region is getting smaller. The amount of the decrease in the exclusion region size from one f bin to the next was determined based on the relative improvement in angular resolution with energy. As described in section 2.2.4, the angular resolution was established by the studies with the Crab Nebula. Figure 4.7 shows the variations in the exclusion region size with energy.

To account for the changing exclusion region size, the number of events collected over a slightly varying area must be normalized to the same area. The collection area of the first f bin was used for this normalization. Therefore M_i was calculated as follows:.

$$M_i = \frac{A_{f1}}{A_{fi}} * M_i'$$

where M_i is the measured event rate, A_{f1} is the area of the first f bin, A_{fi} is the area of the f bin and M_i' is the measured event rate for the f bin. Using this method to remove the sources from the diffuse emission, the significance of the diffuse emission was 4.7σ above the background. This increase in significance is due to the exclusion region used, which only contain 68% of the emission from the sources. It also did not take into account the extension of the two Milagro sources. MGRO J2019+37 has an extension of 1.1 ± 0.5 deg and MGRO J2031+41 has a extension of 3.0 ± 0.9 deg [10]. Therefore, a third study was performed where the extension of the sources was added to the exclusion region:

$$D = x + d$$

where d is the size of the varying exclusion region and x is the extension of the source. Figure 4.8 shows the exclusion regions assuming the extension of the sources.

Using this method, a large portion of the Cygnus region was removed. The significance of the diffuse emission is 2.2σ above the background, which is slightly more than the fixed
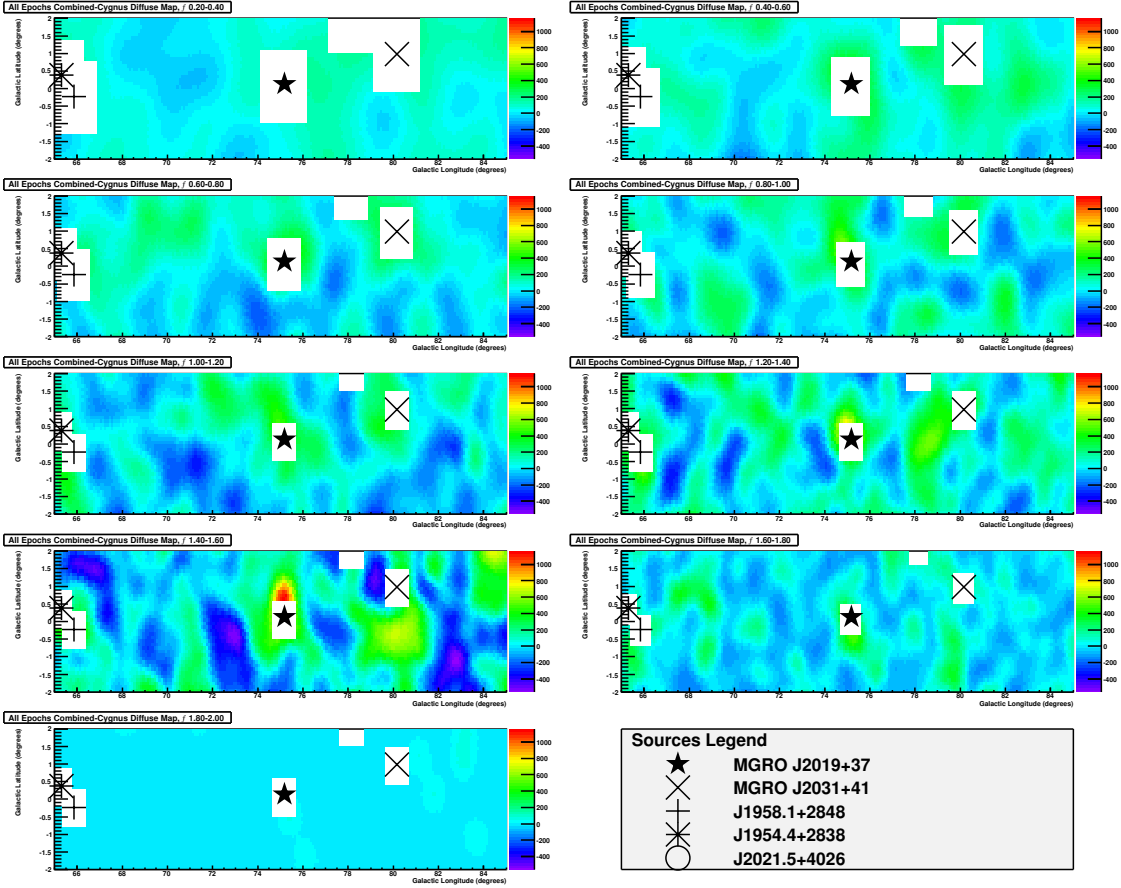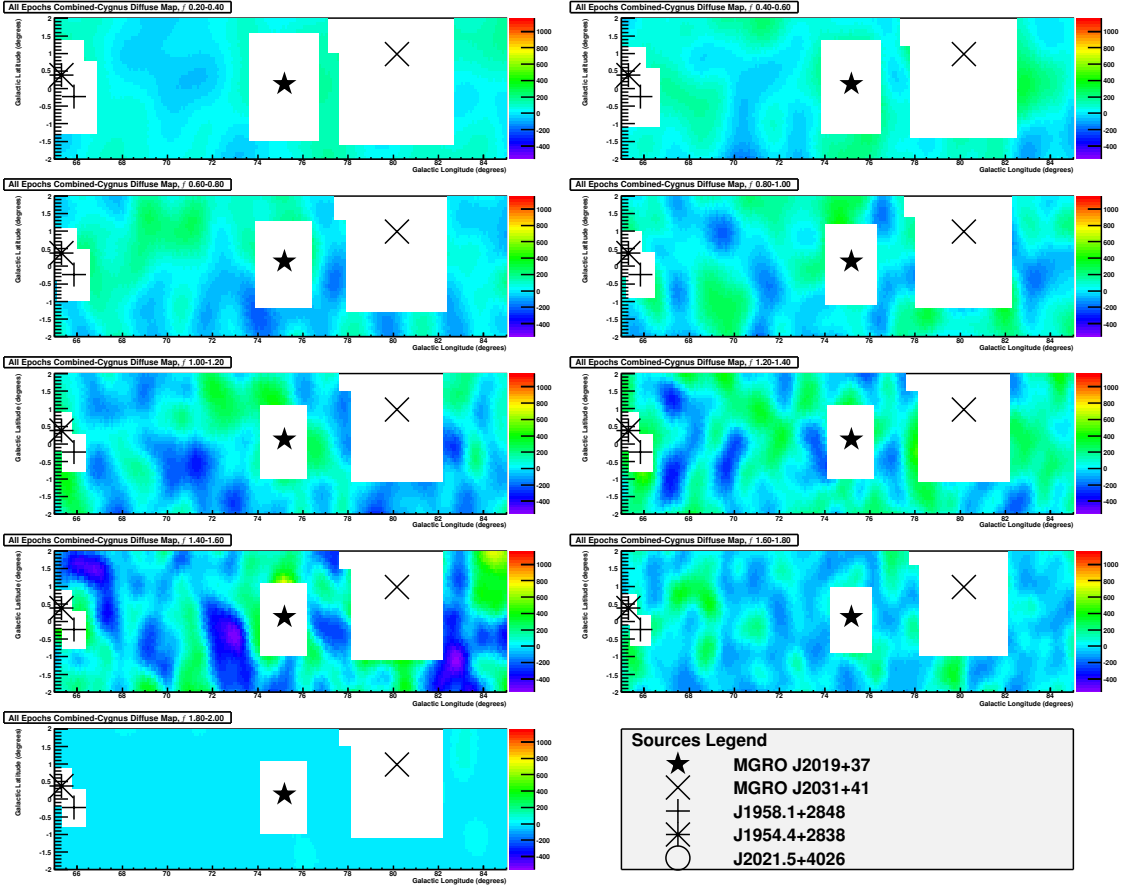
Figure 4.8: Smoothed map of the entire Cygnus region for the nine f that were used in the analysis. The source exclusion region sizes include the extension of MGRO J2019+37 and MGRO J2031+41 as well the variation in angular resolution with f bin.

exclusion region.

The fitting method applied to the diffuse emission produced results with large uncertainties because of the low significance of the diffuse emission. No conclusive statement can be made about the spectrum of diffuse TeV gamma-ray emission from the Cygnus region at this point in the analysis.

Table 4.4
Fit Results for MGRO J2019+37

Fit Parameters for MGRO J2019+37						
Fit	α	I_o (x10^{-10} TeV^{-1} s^{-1} m^{-2})	E_c (TeV)	χ^2	DOF	Probability
W/ Cutoff	2.30 (1.40-2.70)	5.66 (4.04-9.54)	50.12 (17.78-251.18)	4.904	6	55.6%
W/O Cutoff	2.75 (2.65-2.85)	4.04 (3.72-4.37)	-	10.605	7	15.7%

4.3   MGRO J2019+37

MGRO J2019+37 is a gamma-ray source located near the middle of the Cygnus region.
Until recently it had not been seen by other very high energy gamma-ray experiments. It
was first published in the Milagro source catalog at a location of l=75° and b=0.2^o with
a extension of 1.1^o. It was found to have a significance of 10.9σ making it the second
brightest source in the Milagro data [9]. After the second Milagro survey, MGRO J2019+37
was found to have a significance of 12.4σ[10].

For this analysis it was assumed that MGRO J2019+37 was a point source. In order to get
all the events from the source, a smoothed skymap was used. Because of the smoothing
process, the measured number of events corresponds to the bin at the location of the source.
The significance of MGRO J2019+37 is calculated to be 11.4σ above the background in
the data set that is analyzed in this work. The fit is preformed for both a cutoff and no
cutoff, and the results are shown in Table 4.4.

Each of the parameters is given, along with a 1 σ error range as previously described. The
projections of the χ^2 phase space are shown in Figure 4.9. Each projection shows 1-5σ
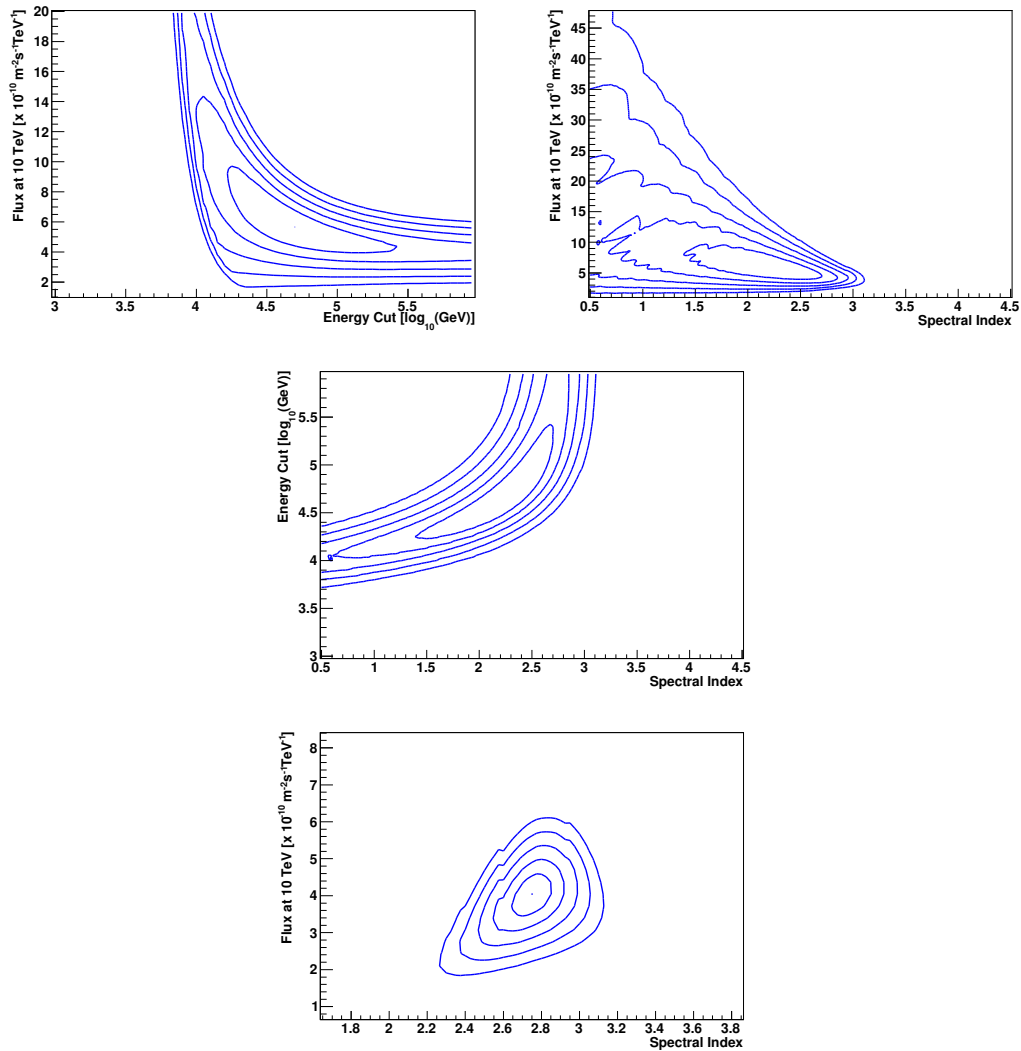
Figure 4.9: Projections of the χ^2 histogram for MGRO J2019+37. Top/Middle: Projections of the 3 dimensional χ^2 space in the case of the spectral fit with a cutoff energy. Bottom: Projection for the spectral fit with no cutoff energy.

contours around the minimum value.

The best fit is with a cutoff energy, but we cannot rule out a spectrum without a cutoff energy for MGRO J2019+37. Figure 4.10 shows the simulated f distributions for the best
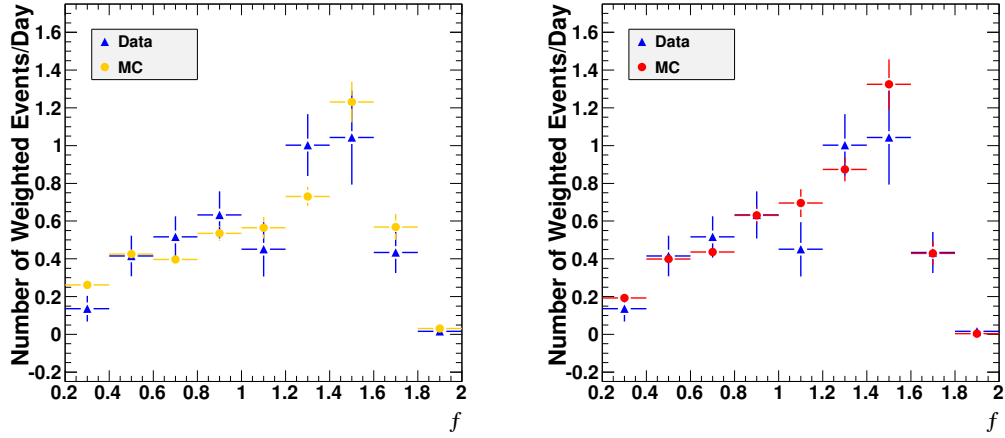
Figure 4.10: f Distributions for MGRO J2019+37. Left: MC and Data event rate for the fit without a cutoff. Right: MC and Data event rate for the fit with a cutoff.

fits compared with the data in blue.

Figure 4.11 shows the two spectra of MGRO J2019+37 in comparison along with their respective 1 and 2 σ error bands. The flux of MGRO J2019+37 at 15 TeV from the fit assuming a cutoff was $1.30x10^{-14}(TeV^{-1}s^{-1}cm^{-2})$ while the flux assuming no cutoff energy was $1.65x10^{-14}(TeV^{-1}s^{-1}cm^{-2})$.

Comparing the flux from MGRO J2019+37 and that of the entire region, it can be seen that MGRO J2019+37 has a flux that contributes $\sim$25% of the flux of the entire regions at 15 TeV. The spectra of both sources are shown in Figure 4.12 without a cutoff and Figure 4.13 with cutoff as well as the previous Milagro diffuse measurement.
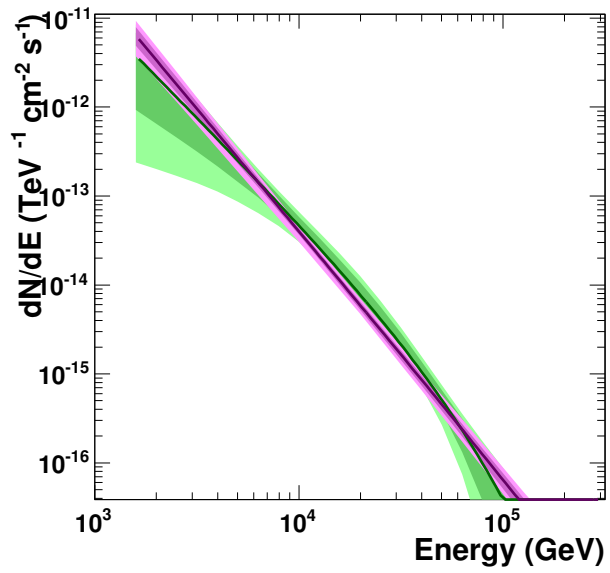
Figure 4.11: Spectrum of MGRO J2019+37 with 1 and 2 σ error bands around best fit. Purple: Fit without cutoff energy. Green: Fit with cutoff energy.

Figure 4.12: Spectra of MGRO J2019+37 and the entire Cygnus region assuming no cutoff energy with 1 σ error band. The black point is the previous Milagro diffuse measurement at 15 TeV with systematic and statistical uncertainties.

Figure 4.13: Spectra of MGRO J2019+37 and the entire Cygnus region assuming a cutoff energy with 1 σ error band. The black point is the previous Milagro diffuse measurement at 15 TeV with systematic and statistical uncertainties.

Chapter 5
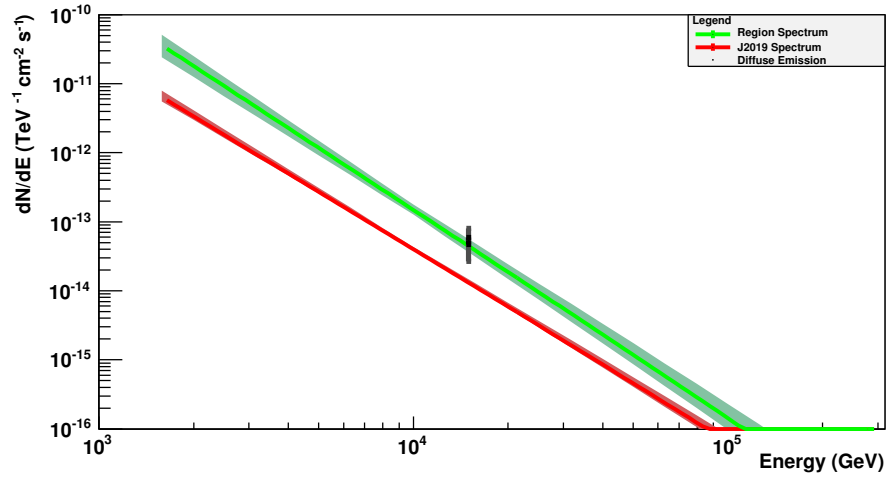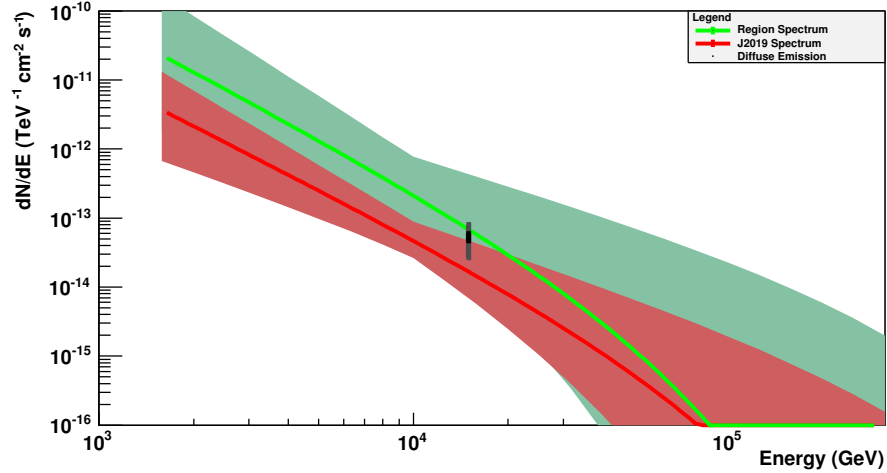
Conclusion

5.1 Discussion

There is no published spectrum for MGRO J2019+37. This first result from the presented

analysis may suggest that the source has a spectrum that is harder than that of the entire

Cygnus region. The flux of MGRO J2019+37 is 25% of the flux from the entire region. The

entire Cygnus region has a flux that is close to that of the previous diffuse measurement.

This may be due to differences in the analysis including variations in data used, sources

taken into account, and spectral index of the analysis.

Error ranges were given for all the parameters which are based on the range of the 1σ

contours. In order to calculate uncertainties the correlation of the parameters needs to be

removed. In the contour plots in Chapter 4, there is a slope to many of the contours which indicates the dependence of one parameter on the other. This correlation can be minimized by changing E_o, or the pivot energy. The pivot energy is the energy that the spectrum is normalized to and adjusting it can minimize the correlation of the parameters. For this analysis the pivot energy was assumed to be 10 TeV but but it has been demonstrated that changing the pivot energy to 2-3 TeV minimizes the correlations between the flux normalization and the spectral index in the case of the fit that assumes an exponential cutoff energy [30].

5.2   Future Work

The next step in the analysis of the Cygnus Region is to account for the changing declination across the region. Given the results of the systematic studies presented in this thesis it is not expected to change the resulting spectra significantly. The analysis of the point sources in the region is nearing completion. The spectral analysis of MGRO J2019+37 has been presented in this thesis and the analysis of MGRO J2031+41 is underway [31]. The ranges and step sizes of the scanning procedure that is used to find the best fit values should be studied further and then optimized. The final stage is to adjust the weights being applied to the skymaps to the spectrum found in the present analysis and compare the resulting morphology to other wavebands.

Fermi has already released more than three years of data, which can be analyzed with publicly available software tools and thus can be combined with Milagro data. Finally, the next generation water Cherenkov detectors, the High Altitude Water Cherenkov (HAWC) experiment is currently under construction in Mexico and when completed will have a sensitivity that is 15 times that of the Milagro observatory. Data from this next experiment will help improve the separation between localized sources and the diffuse emission which will help with the spectral analysis of these two contributions.

References

[1] NASA/JPL-Caltech/R. Hurt. (2011) Wikipedia: The Milky Way. [Online]. Available: http://en.wikipedia.org/wiki/Milky_Way

[2] Los Alamos National Laboratory. (2011) Physics Division: The Milagro Gamma-Ray Observatory. [Online]. Available: http://www.lanl.gov/milagro/index.shtml

[3] A. A. Abdo, "Discovery of Localized TeV Gamma-Ray Sources and Diffuse TeV Gamma-Ray Emission from the Galactic Plane with MILAGRO Using a new Background Rejection Technique," Ph.D. dissertation, Michigan State University, 2007.

[4] A. A. Abdo *et al.*, "Observation and Spectral Measurements of the Crab Nebula with Milagro," unpublished.

[5] ——, "Discovery of TeV Gamma-Ray Emission from the Cygnus Region of the Galaxy," *The Astrophysical Journal*, vol. 658, pp. L33–L36, 2007.

[6] Y. M. Butt *et al.*, "Deeper Chandra Follow-up of Cygnus TeV Source Perpetuates Mystery," *The Astrophysical Journal*, vol. 643, pp. 238–244, 2006.

[7] N. J. Wright and J. J. Drake, "The Massive Star-Forming Region Cygnus OB2. I. Chandra Catalog of Association Members," *The Astrophysical Journal Supplement*, vol. 184, pp. 84–99, 2009.

[8] F. Camilo *et al.*, "Radio Detection of LAT PSRs J1741-2054 and J2032+4127: No Longer Just Gamma-ray Pulsars," *The Astrophysical Journal*, vol. 705, pp. 1–13, 2009.

[9] A. A. Abdo *et al.*, "TeV Gamma-Ray Sources from a Survey of the Galactic Plane with Milagro," *The Astrophysical Journal*, vol. 664, pp. L91–L94, 2007.

[10] ——, "Milagro Observations of Multi-TeV Emission from Galactic Sources in the Fermi Bright Source List," *The Astrophysical Journal*, vol. 700, pp. L127–L131, 2009.

[11] J. M Paredes *et al.*, "Radio continuum and near-infrared study of the MGRO J2019+37 region," *Astronomy and Astrophysics*, vol. 507, pp. 241–250, 2009.

[12] E. Aliu, "VERITAS discovery of complex emission towards Cyg OB1," Fermi Symposium Poster, May 2011.

[13] S. D. Hunter *et al.*, "EGRET Observations of the Diffuse Gamma-Ray Emission from the Galactic Plane," *The Astrophysical Journal*, vol. 481, pp. 205–240, 1997.

[14] F. Aharonian *et al.*, "Discovery of very-high-energy γ-rays from the Galactic Centre Ridge," *Nature*, vol. 439, pp. 695–698, 2006.

[15] A. A. Abdo *et al.*, "Fermi LAT Observation of Diffuse Gamma Rays Produced Through Interactions Between Local Interstellar Matter and High-energy Cosmic Rays," *The Astrophysical Journal*, vol. 703, pp. 1249–1256, 2009.

[16] ——, "Spectrum of the Isotropic Diffuse Gamma-Ray Emission Derived from First-Year Fermi Large Area Telescope Data," *Physical Review Letters*, vol. 104, p. 101101, 2010.

[17] A. W. Strong, I. V. Moskalenko, and O. Reimer, "A New Determination of the Extragalactic Diffuse Gamma-Ray Background from EGRET Data," *The Astrophysical Journal*, vol. 613, pp. 956–961, 2004.

[18] ——, "Diffuse Galactic Continuum Gamma Rays: A Model Compatible with EGRET Data and Cosmic-Ray Measurements," *The Astrophysical Journal*, vol. 613, pp. 962–976, 2004.

[19] A. A. Abdo *et al.*, "Measurement of the Cosmic Ray $e^+ + e^-$ Spectrum from 20GeV to 1TeV with the Fermi Large Area Telescope," *Physical Review Letters*, vol. 102, p. 181101, 2009.

[20] ——, "A Measurement of the Spatial Distribution of Diffuse TeV Gamma-Ray Emission from the Galactic Plane with Milagro," *The Astrophysical Journal*, vol. 688, pp. 1078–1083, 2008.

[21] F. Aharonian *et al.*, "HESS Observations of the Galactic Center Region and Their

Possible Dark Matter Interpretation," *Physical Review Letters*, vol. 97, p. 221102, 2006.

[22] X. J. Bi *et al.*, "The Diffuse GeV-TeV γ-Ray Emission of the Cygnus Region," *The Astrophysical Journal*, vol. 695, pp. 883–887, 2009.

[23] E. Hays, "A Search for TeV Emission from Active Galaxies using the Milagro Observatory," Ph.D. dissertation, University of Maryland, 2004.

[24] T. K. Gaisser *et al.*, "Gamma-ray Astronomy above 50 TeV with Muon-poor Showers," *Physical Review D*, vol. 43, pp. 314–318, 1991.

[25] T. P. Li and Y. Q. Ma, "Analysis methods for results in Gamma-ray Astronomy," *The Astrophysical Journal*, vol. 272, pp. 317–324, 1983.

[26] R. Atkins *et al.*, "Observation of TeV Gamma Rays from the Crab Nebula with Milagro Using a New Background Rejection Technique," *The Astrophysical Journal*, vol. 595, pp. 803–811, 2003.

[27] D. Heck *et al.*, "CORSIKA: A Monte Carlo code to Simulate Extensive Air Showers," *Forschungszentrum Karlsruhe (FZKA)*, vol. 6019, 1998.

[28] Geant4 Collaboration, "Geant4-A Simulation Toolkit," *Nuclear Instruments and Methods in Physics Research Section A*, vol. 506, pp. 250–303, 2003.

[29] F. Aharonian *et al.*, "Observations of the Crab nebula with HESS," *Astronomy and Astrophysics*, vol. 457, pp. 899–915, 2006.

[30] E. Bonamente, Private Communication, 2011.

[31] E. Leonard, Private Communication, 2011.